UC Irvine
ICTS Publications

Title

Characterization of Cholesterol Crystals in Atherosclerotic Plaques Using Stimulated Raman Scattering and Second-Harmonic Generation Microscopy

Permalink

https://escholarship.org/uc/item/8n6841fj

Journal

Biophysical Journal, 102(8)

ISSN

1542-0086

Authors

Suhalim, Jeffrey L.
Chung, Chao-Yu
Lilledahl, Magnus B.
et al.

Publication Date

2012-04-18

Peer reviewed

Characterization of Cholesterol Crystals in Atherosclerotic Plaques Using Stimulated Raman Scattering and Second-Harmonic Generation Microscopy

Jeffrey L. Suhalim,[†‡] Chao-Yu Chung,[§] Magnus B. Lilledahl,[¶] Ryan S. Lim,[†] Moshe Levi,[‖] Bruce J. Tromberg,[†‡] and Eric O. Potma[†§*]

[†]Beckman Laser Institute, [‡]Department of Biomedical Engineering, and [§]Department of Chemistry, University of California, Irvine, California; [¶]Department of Physics, Norwegian University of Science and Technology, Trondheim, Norway; and [‖]Division of Renal Diseases and Hypertension, Department of Medicine, University of Colorado Denver, Aurora, Colorado

ABSTRACT   Cholesterol crystals (ChCs) have been identified as a major factor of plaque vulnerability and as a potential biomarker for atherosclerosis. Yet, due to the technical challenge of selectively detecting cholesterol in its native tissue environment, the physiochemical role of ChCs in atherosclerotic progression remains largely unknown. In this work, we demonstrate the utility of hyperspectral stimulated Raman scattering (SRS) microscopy combined with second-harmonic generation (SHG) microscopy to selectively detect ChC. We show that despite the polarization sensitivity of the ChC Raman spectrum, cholesterol monohydrate crystals can be reliably discriminated from aliphatic lipids, from structural proteins of the tissue matrix and from other condensed structures, including cholesteryl esters. We also show that ChCs exhibit a nonvanishing SHG signal, corroborating the noncentrosymmetry of the crystal lattice composed of chiral cholesterol molecules. However, combined hyperspectral SRS and SHG imaging reveals that not all SHG-active structures with solidlike morphologies can be assigned to ChCs. This study exemplifies the merit of combining SRS and SHG microscopy for an enhanced label-free chemical analysis of crystallized structures in diseased tissue.

INTRODUCTION

The accumulation of lipids in the arterial blood vessel wall, resulting in the formation of lipid-rich plaques, is a prominent feature of atherosclerosis. Atherosclerotic plaques can erode or rupture, which has been recognized as a universal pathological precursor of myocardial infarction and stroke—two major causes of death in many Western countries (1–3). The physicochemical properties of lipids play a prominent role in atherosclerotic disease progression. Hence, understanding the role of lipids in plaque development and rupture is vital for devising therapeutic strategies for atherosclerosis.

Various studies have pointed out the correlation between lipid content, including cholesterol and cholesteryl esters, and the severity of the disease (4,5). It has been shown that cholesterol crystals (ChCs) pierced the arterial intima of patients who experienced acute coronary death. On the other hand, patients who suffered a noncardiac-related death did not manifest arterial perforation by ChCs, despite having severe atherosclerosis (6–9). These observations underline the link between presence of ChCs and acute coronary death. More recently, the capability of ChC to induce inflammation and its correlation with plaque area and presence of macrophage-derived matrix metalloproteinase have been demonstrated (10–12), highlighting the role of ChC in cellular processes known to exacerbate plaque vulnerability (3,13,14). Furthermore, it has been

suggested that solid ChC structures are also capable to physically perforate cell membranes and the plaque's fibrous cap, which could subsequently trigger cell apoptosis and plaque rupture, respectively (7). Despite the importance of ChC in atherosclerotic disease progression, the biophysical and chemical events responsible for ChC formation and the subsequent role of ChC in plaque aggravation remain largely unknown. Hence, the ability to selectively detect ChC within its native milieu in the lesion may provide insights into the progression of ChC and atherogenesis.

Standard light microscopy has been used extensively to examine arterial tissues. The presence of ChCs has often been inferred from empty spaces exhibiting rodlike structure in the optical image, which are presumably the result of dissolving ChCs with the addition of dehydrating agents (9). In more recent studies, confocal reflection microscopy and micro-optical coherence tomography (micro-OCT) have been utilized to visualize ChC (11,15). Although confocal reflection microscopy and micro-OCT are sensitive to the enhanced reflectivity of ChC, both techniques are not chemically selective and thus cannot conclusively discriminate ChC from other crystallized materials in the plaque. Similarly, lipophilic stains such as Sudan Black and Nile Red lack accuracy and specificity (16,17). Such shortcomings compromise the precise identification and quantification of ChC, limiting the use of ChC as a biomarker for atherosclerotic disease.

The contrast in nonlinear optical (NLO) microscopy, on the other hand, is typically derived from optical properties of endogenous compounds, avoiding the need for exogenous

dyes and allowing three-dimensional visualization of structures with submicron resolution (17,18). In particular, coherent Raman techniques such as coherent anti-Stokes Raman scattering (CARS) and stimulated Raman scattering (SRS) provide label-free detection of lipophilic compounds based on the intrinsic vibrational signatures of the molecules (19,20). In recent work, we have successfully used hyperspectral CARS imaging, where each pixel in the image carries information in the spectral dimension, for the identification of ChC within intact mouse aortas (20).

The spectral sensitivity of CARS enabled a clear discrimination between ChC and structures with similar morphologies. However, a detailed spectroscopic analysis of ChCs in their native plaque environment is not straightforward using CARS, due to the presence of a nonresonant electronic background (18,21). To evaluate the potential of NLO microscopy for the study of cholesterol in atherosclerosis, a more elaborate analysis of the effects of ChC orientation, crystal variability, and the crystal's immediate surroundings on the detection sensitivity of NLO is needed.

In this work, we provide a comprehensive study of ChC in atherosclerotic plaques with NLO microscopy. To facilitate the spectral analysis, we employ hyperspectral SRS microscopy. Unlike CARS, SRS is devoid of the nonresonant electronic background (18,21), which enables a direct comparison of the ChC spectra with the Raman spectra of in vitro standards. In addition, we examine the second-order nonlinearity of ChCs with second-harmonic generation (SHG) microscopy. SHG is exclusively sensitive to noncentrosymmetric materials such as chiral crystals, and thus can be used to complement hyperspectral SRS in discriminating ChCs from other amorphous lipids. We will show that the combined SRS/SHG method is a promising approach for identifying and interrogating cholesterol crystals and its derivatives in atherosclerotic plaques.

MATERIALS AND METHODS

SRS and SHG imaging

The Stokes and pump beams used in the SRS experiments were derived from an optical parametric oscillator (OPO; Levante Emerald, Berlin, Germany) pumped by a 7-ps, 76-MHz mode-locked Nd:vanadate laser (Picotrain; High-Q, Hohenems, Austria). The Stokes beam was fixed at 1064 nm, whereas the pump beam was tuned within the 800–820-nm range. Tuning was accomplished through computer control of the crystal temperature, Lyot filter, and cavity length of the OPO. The pump and Stokes beams were overlapped both spatially and temporally on a dichroic beam combiner, and sent into a laser scanner (Fluoview 300; Olympus, Center Valley, PA), illuminating the specimen with a 20×, 0.75 NA objective lens (UPlanSApo; Olympus) mounted on an inverted microscope (IX71; Olympus).

To monitor stimulated Raman loss, the Stokes beam was modulated at 10 MHz with an acoustic optical modulator (Crystal Technology, Palo Alto, CA). The modulated pump intensity was detected by a photodiode (FDS1010; Thorlabs, Newton, NJ), and the signal was demodulated with a home-built lock-in amplifier. SHG signals induced by the pump beam were measured in both forward- and epi-direction through a bandpass filter

(400 ± 40 nm; Thorlabs) with a photomultiplier tube (R3896; Hamamatsu, Hamamatsu City, Japan). We note that no autofluorescence of pure cholesterol crystals was observed within the spectral detection window. The average combined power of Stokes and pump at the specimen was kept under 30 mW throughout this study to ensure sample integrity.

Spectral and polarization analysis

The concept of hyperspectral coherent Raman imaging based on picosecond laser source has been discussed in several recent works (22,23), including our own (20,24). To achieve rapid hyperspectral imaging from 2750 to 3050 cm^{-1}, with spectral resolution of ~5 cm^{-1} (full width half-maximum), several parameters of the OPO, including crystal temperature, Lyot filter, and cavity length, were automatically tuned with homemade software written in Python (http://python.org/). At each wavelength, an SRS image was registered within a fixed field of view, whereas the output power from the OPO was maintained at a constant level. The fastest implementation of hyperspectral SRS imaging with our setup produces data stacks of at least 50 spectral points in 10–15 min, corresponding to an effective spectral acquisition time of 2.3–3.5 ms per pixel. Consequently, each pixel in the image contains an SRS spectrum that can be directly compared to Raman signatures available in the literature or obtained in vitro.

Principal component analysis (PCA) was implemented to identify regions in the image with distinct spectral signatures. Briefly, PCA is an unsupervised statistical method that enables multidimensional datasets (i.e., 512 × 512 pixels acquired at 50 different spectral points) to be analyzed and visualized in terms of fewer variables (i.e., most significant variations in the dataset can be captured with 3–4 variables). A more detailed description of PCA for spectral analysis can be found in the literature (20,25,26). SRS spectra were analyzed using ImageJ (U.S. National Institute of Health, Bethesda, MD) and MATLAB (The MathWorks, Natick, MA). A commercial confocal Raman microscope with excitation wavelength of 532 nm (InVia Confocal; Renishaw, Wotton-under-Edge, Gloucestershire, UK) was utilized to acquire Raman spectra of cholesterol monohydrate.

The polarization dependence of the SRS and SHG signals was measured by controlling the polarization orientation of the linearly and parallel polarized pump and Stokes beams. An achromatic half-wave plate was utilized to control the input polarization of both pump and Stokes beams. The signal was collected as a function of the input polarization without the use of an analyzer. The average pixel intensity within a region of interest (ROI) in each image was extracted using ImageJ, and plotted using the Radar Chart Function in Microsoft Excel (Microsoft, Redmond, WA).

Specimen and sample preparation

5/6 nephrectomized ApoE-deficient mice (ApoE−/−; stock No. 002052) were purchased from Jackson Laboratory (Bar Harbor, ME). At eight weeks of age, the mice were fed a Western-style diet (0.15% cholesterol and 21% milk fat; TD88137; Harlan Teklad, Indianapolis, IN). After 16 weeks of Western diet, whole intact aortas were harvested, incised longitudinally, and placed on a microscope slide with the luminal side exposed to allow en face imaging. The specimens were fixed with 2%-paraformaldehyde, and phosphate-buffered saline was applied before sandwiching the aorta with glass coverslips. Animal experiments were approved by the Institutional Animal Care and Research Advisory Committee of the University of Colorado at Denver.

Cholesterol was purchased from Sigma-Aldrich (St. Louis, MO) and used without further purification. Cholesterol monohydrate crystals were synthesized by recrystallizing cholesterol in water. The crystals were transferred to a glass coverslip for subsequent microspectroscopic analysis. Raman spectra of protein and other cholesterol derivatives were obtained from http://www.sigmaaldrich.com/, and used as a reference for spectral analysis.

RESULTS

Cholesterol identification via hyperspectral SRS imaging

To characterize the vibrational spectral signature of ChC, we performed hyperspectral SRS in the CH stretching vibrational region (2700–3100 cm^{-1}) on isolated ChCs in vitro, obtained through recrystallization of cholesterol in water. The Raman spectrum shows several distinct peaks, including prominent peaks at 2855 cm^{-1}, 2869 cm^{-1}, 2907 cm^{-1}, 2945 cm^{-1}, and 2966 cm^{-1} (Fig. 1 A). All of the spectral signatures of ChC in this range are reproduced in the average SRS spectrum.

Spectral variation was observed among the crystals (Fig. 1 A). This variation was found to correlate strongly with the polarization of the excitation beams. In particular, the spectral region near the 2855 cm^{-1} and the 2869 cm^{-1} bands is highly polarization-dependent. In addition, the 2945 cm^{-1} band exhibits a polarization dependence orthogonal to the former bands. On the other hand, the peak at 2907 cm^{-1} is relatively insensitive to the input polarization (Fig. 1 B). This polarization sensitivity of the CH stretching band suggests that ChCs, which are arbitrarily oriented in tissue, may display similar polarization-dependent spectral variations. Thus, it is important to account for the polarization effects on the spectral signature when assigning the crystal's composition.

In the mouse aorta, lipid-rich structures with solidlike morphologies were identified. In particular, various sharp and rectangular structures were observed, including plate-

and needle-shaped structures (Fig. 2, A and D). The extracted SRS spectra of these tissue structures are shown in Fig. 2, C and F. The solidlike structures exhibit a spectral profile that is virtually identical to the spectral signatures of ChC in vitro shown in Fig. 1 A.

SHG signal from cholesterol crystal

The corresponding SHG images in Fig. 2 are shown in panels B and E. The fact that the condensed structures with strong SRS signals also exhibit strong SHG signal indicates that these structures are highly ordered on the molecular level. No significant autofluorescence from structures identified as ChC was observed within the spectral detection window (data not shown), corroborating that bright spots in the SHG images were indeed generated through second-harmonic activity of the molecules.

In Fig. 3, A and B, an SRS image and SHG image of an area rich in lipid structures are shown. Several structures are selected and the corresponding SRS spectra are given in Fig. 3 C. Structures that exhibited spectra with the three distinct ChC peaks at 2869 cm^{-1}, 2907 cm^{-1}, and 2945 cm^{-1} showed a strong SHG response. The spectra corresponding to the ChC rich areas with SHG activity are given in blue. This confirms that ChC structures display a nonvanishing SHG signature. On the other hand, the spectra indicated with a solid black line in Fig. 3 C showed a relatively strong SRS response but produced a very weak signal in the SHG channel. It can be seen that the spectra of these regions of interest (ROIs) are devoid of the three characteristic ChC peaks and thus do not correspond to ChC-rich structures. For instance, the ROI 3 shows a characteristic amorphous aliphatic lipid spectrum, which has a strong SRS signal but is not expected to have any SHG activity. These observations provide strong evidence that crystallized ChC materials in the atherosclerotic lesion are SHG-active, whereas other amorphous lipid-rich materials are SHG-inactive.

Polarization dependence of cholesterol crystal

To further study the nature of the ChC-rich structures, the intensity of the SRS and SHG signals was measured as a function of laser polarization. In Fig. 4, a comparison between the polarization dependence of the SRS and SHG signals is shown for different ROIs. The SRS (red) and SHG (blue) signals measured in ROI 4 and ROI 5 are polarization-sensitive. It can be seen that the polarization dependence of SHG signal from ROI 4 is more prominent than ROI 5. Note that the maximum SHG intensities of ROI 4 and ROI 5 are at different polarization angles than the maximum SRS intensities. Because SRS and SHG signals originate from two independent processes, polarization angles at which maximum SHG and SRS intensities occur do not necessarily correlate. The observed polarization
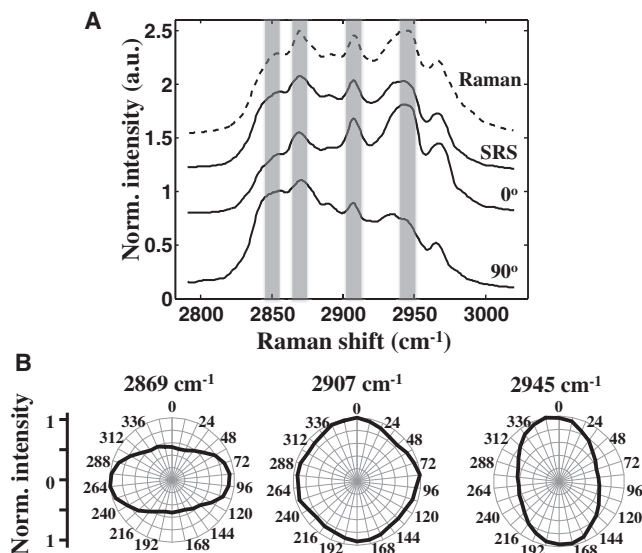

FIGURE 1 Vibrational signature of ChC. (A) Average spectra of isolated ChC in vitro obtained with a Raman microscope (dashed line). Spectra were averaged based on eight point measurements. SRS spectra at two different laser polarizations (bottom solid lines). Average of SRS spectra at 0° and 90° (top solid line). (B) Relative intensities of selected Raman peaks acquired at different laser polarizations.
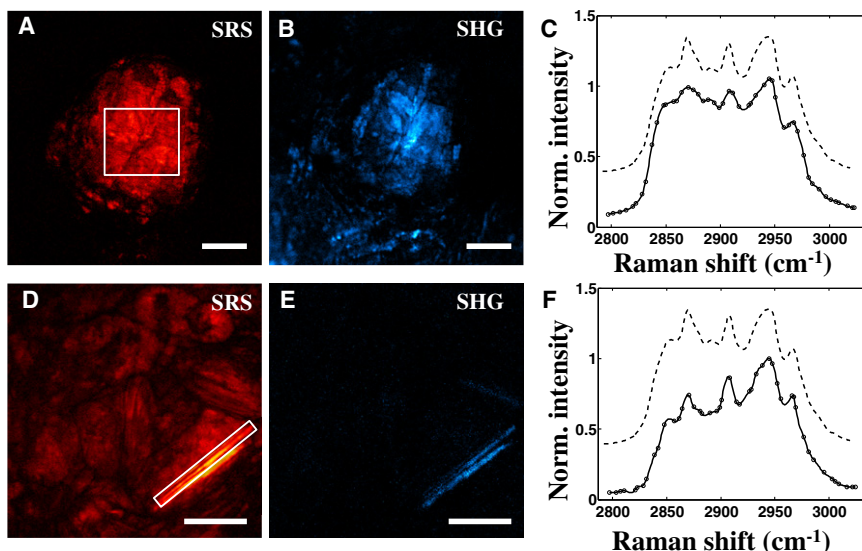
FIGURE 2 Identification of ChCs in athero-sclerotic plaques of ApoE$^{-/-}$ mouse. Plate- and needle-shaped structures can be visualized in SRS (A and D, respectively) and SHG (B and E, respectively) channels. SRS images were acquired at 2855 cm^{-1}. SRS spectra from highlighted regions in A and D are plotted in panel C and F, respectively (solid lines). Raman spectra from isolated ChC are provided as a reference (dashed lines). Scale bars: 25 μm.

dependence nonetheless suggests that the molecules in the ChC-rich structures are highly ordered.

The SRS signal from ROI 3 has a much weaker polarization dependence relative to ROI 4 and ROI 5. As predicted by the SRS spectral analysis above, the amorphous aliphatic lipids in ROI 3 exhibit virtually no SHG signal (Fig. 3 B). These observations confirm that the lipids in ROI 3 are
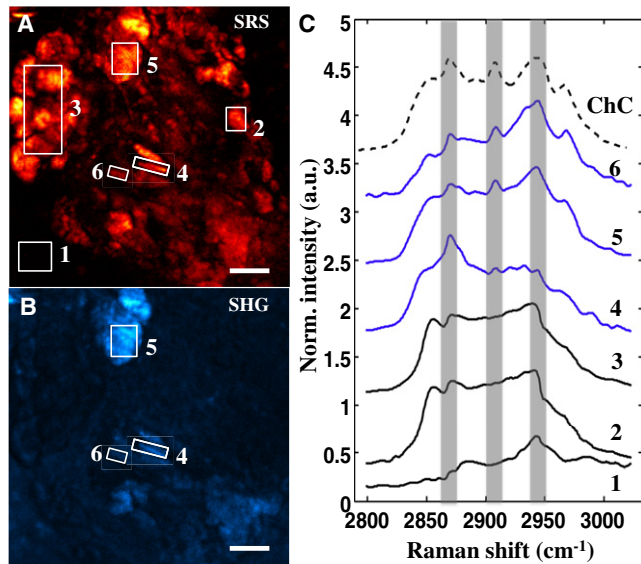

FIGURE 3 Spectral analysis of plaque components. Maximum projections of SRS (A) and SHG (B) images acquired at consecutive laser polarizations of lipid-rich area in the plaque. (C) SRS spectra extracted from ROIs highlighted in panel A are plotted. ROIs 4–6 are SHG-active, as evident in panel B, and exhibit spectra (solid lines) consistent with the spectral signature of ChC (dashed line). In contrast, amorphous lipophilic compounds in ROI 3 exhibit virtually no SHG signal, indicating lack of preferential orientation. The background signal in the SHG channel can be attributed to residual autofluorescence from the surrounding tissue matrix. Scale bars: 10 μm.
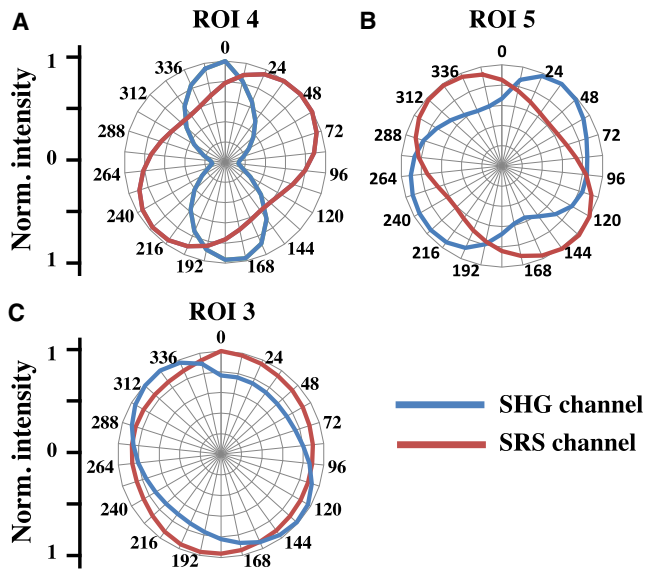
amorphous and noncrystalline in nature. The weak background signal and polarization dependence in the SHG channel can be attributed to residual autofluorescence from the surrounding tissue matrix.

Chemical selectivity of SHG

To explore the specificity of SHG for cholesterol detection, SRS spectra from different ROIs were analyzed. The spectral analysis in Fig. 3 suggests that SHG-activity is exclusive to ChC-rich structures. However, condensed needle-shaped structures, which display SHG-activity but have spectra different from the spectral signature of cholesterol monohydrate crystals, were also observed. An example is shown in Fig. 5. The structure in the white ROI has a strong SRS and SHG response. Nonetheless, peaks are observed at 2898 cm^{-1} and 2937 cm^{-1} that do not correspond to the peaks of cholesterol monohydrate crystals (top dashed spectrum in Fig. 5 C). For comparison, the Raman spectrum of cholesteryl oleate is also given in Fig. 5. The similarity between the spectra from ROI and from cholesteryl oleate suggests that the condensed structure is a cholesteryl ester crystal rather than a cholesterol monohydrate crystal. In addition, needles with spectral signature similar to cholesteryl linoleate were observed (data not shown). These observations underline that more crystalline materials found in plaques exhibit SHG activity besides cholesterol monohydrate crystals.

In addition to the SHG response of crystallized cholesterol and cholesteryl esters, SHG signals from other tissue components was observed. In Fig. 6, the chemical makeup of SHG-active regions with distinct morphologies is compared. A plate-shaped structure that shows strong SRS and SHG signals is seen (Fig. 6, A and B, respectively). The SRS spectral signature extracted from the plate

A ROI 4

B ROI 5

C ROI 3

SHG channel
SRS channel

FIGURE 4 Polarization dependence of ChC. SRS microscope was tuned to the CH_2 symmetric stretch (at 2855 cm^{-1}) to visualize lipid-rich materials. Polar plots of ROIs 3–5 highlighted in Fig. 3 A are shown. (*Red and blue lines*) Intensities from SRS and SHG channels, respectively. Materials in ROIs 4 and 5, which were identified as ChCs (Fig. 3 C), are SHG-active. Additionally, both SRS and SHG signals are highly polarization-dependent, corroborating the crystallinity of the materials. In contrast, amorphous lipid-rich materials in ROI 3 exhibit no SHG signal and have weak polarization dependence, indicating lack of preferential orientation.

features spectral peaks corresponding to the Raman spectrum of ChC (Fig. 6 D; *blue solid spectrum* versus *black dashed spectrum*, respectively). In contrast, the SRS spectral signature extracted from the SHG-active area below the plate-shaped structure (*solid magenta spectrum*) is consistent with the spectral signature of structural proteins (27,28). The SHG activity in this area can be attributed to the presence of collagen fiber (28,29). A decomposition map based on PCA was constructed to highlight the distribution of pixels with ChC and protein signature (Fig. 6 C). Furthermore, needle-shaped protein-rich structures with intense SHG-signals were observed as well (data not shown). These observations exemplify that the SHG signal observed in atherosclerotic plaques is not exclusive to crystals of cholesterol monohydrate or cholesteryl esters.

DISCUSSION

ChC has been gaining importance in the atherosclerosis research community, with observations suggesting that these crystals are capable of inducing inflammation—a hallmark of atherogenesis—and physically penetrating the fibrous cap, which consequently could increase the likelihood of plaque rupture (7,10–12). Hence, the ability to selectively detect ChC within intact arterial tissue is significant. Previous optical microscopy studies have utilized either confocal reflection microscopy or micro-OCT to identify ChC (11,15). These two techniques are sensitive to the enhanced reflectivity of ChC, however, both techniques are not chemically selective, and thus cannot discriminate ChC from other crystallized materials in the plaque. To this end, vibrational Raman signatures of endogenous molecules can be used to visualize and identify the chemical makeup of various plaque components (18,30). In our recent work, we have implemented this concept, specifically by hyperspectral CARS imaging, and observed spectral variations among structures with similar morphologies, including crystallized structures (20). Nonetheless, deducing the specific composition based on CARS spectra is challenging due to the presence of the nonresonant background, which distorts the spectral signatures and requires advanced postprocessing to retrieve the Raman profiles (18,27,31–34).

In this study, we employed a hyperspectral imaging scheme based on SRS, which enables a direct comparison between Raman spectra of known lipid constituents in the atherosclerotic plaques without spectral postprocessing. Our study confirms that cholesterol can be reliably detected with coherent Raman imaging techniques. The strong similarity between the retrieved spectra from condensed crystallike structures in the lesion and the Raman spectrum of cholesterol monohydrate crystal in vitro indicates that ChC in atherosclerotic plaques can be readily identified based on its spectral signatures and solidlike morphology.

The Raman spectrum of ChC in the C-H stretching vibrational range features a series of signatures that can be attributed to CH_2 and CH_3 stretches of cholesterol. The Raman peak at 2855 cm^{-1} can be confidently assigned to the symmetric CH_2 stretching mode (35–37). The mode near 2869 cm^{-1} has been ascribed to the symmetric CH_3 stretch, and the peak at 2966 cm^{-1} has been attributed to the
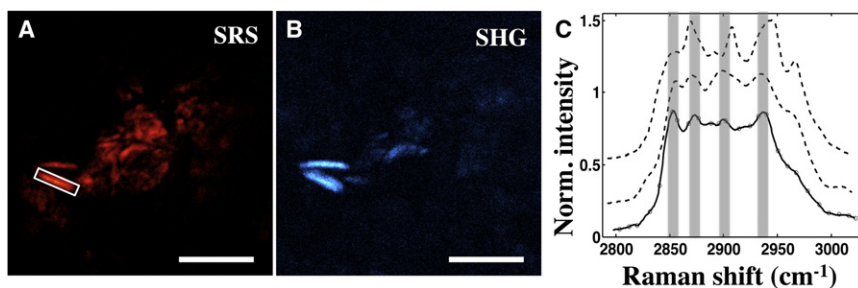

FIGURE 5 SHG is not chemically selective. (*Rectangular box*) Plaque crystal, observed in both SRS (A) and SHG (B) channels, exhibits characteristic spectra (*solid line* in panel C) different from spectral signature of ChC (*top dashed line*). SRS image was acquired at 2855 cm^{-1}. The spectrum of cholesteryl-oleate is provided for comparison (*bottom dashed line*). Scale bars: 10 μm.
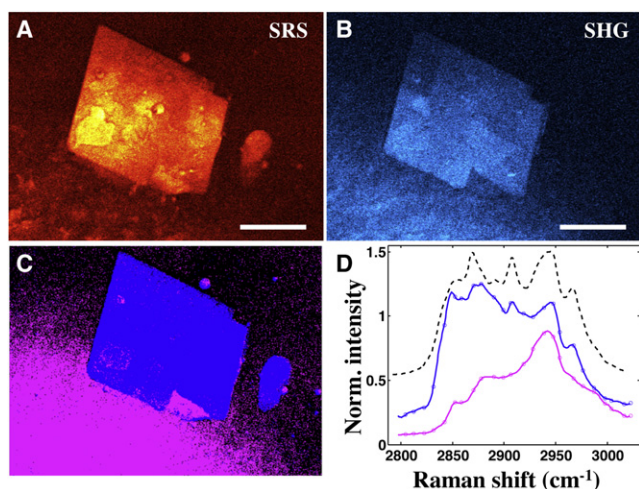
FIGURE 6 SHG signal is not exclusive to crystallized cholesterol. SRS (*A*) and SHG (*B*) images of platelike structure within an atherosclerotic plaque are shown. SRS image was acquired at 2855 cm^{-1}. Panel *C* is a PCA decomposition map: pixels exhibiting spectral signature of ChC (*blue*) and structural protein (*magenta*), respectively. SRS spectra (*blue* and *magenta pixels*) are plotted in panel *D*. Not all structures with ChC spectral signature are SHG-active, illustrating the presence of amorphous cholesterol (*circular blue structure*). Other SHG-active materials (*magenta pixels*) exhibit a typical structural protein spectrum, which can be attributed to presence of collagen in the tissue. Scale bars: 30 μm.

asymmetric CH$_3$ stretch. The region between 2869 cm^{-1} and 2945 cm^{-1} is more ambiguous due to the presence of combination bands (35,36). Bresson et al. (36) identified the 2907 cm^{-1} mode as an asymmetric CH$_2$ stretching vibration, whereas the mode near 2945 cm^{-1} was attributed to a combination band. Table 1 summarizes the frequencies and possible assignments of the C-H stretching bands of cholesterol.

Although all ChCs in the plaque exhibited the distinct vibrational signatures listed in Table 1, the relative intensities of the bands changed from crystal to crystal. Our polarization studies on ChCs in the plaque and ChCs grown in vitro confirm that these spectral intensity changes are due to the orientation of the modes relative to the polarization orientation of the excitation light. Among the modes identified, the region near the symmetric CH$_2$ mode vibration ($\sim$2855 cm^{-1}) and the 2945 cm^{-1} mode show a strong polarization dependence, whereas the other modes are relatively insensitive to the polarization orientation of the exci-

TABLE 1 Raman bands assignment of ChC

Peak position	CH stretching modes
2855 cm^{-1}	CH$_2$ symmetric
2869 cm^{-1}	CH$_3$ symmetric
2907 cm^{-1}	CH$_2$ asymmetric
2945 cm^{-1}	CH$_3$ symmetric or CH$_2$ asymmetric
2966 cm^{-1}	CH$_3$ asymmetric

Values from Faiman (35) and Bresson et al. (36).

tation beams. The crystal structure of the cholesterol molecule shows a relatively planar configuration, in which the polarizability axis of the symmetric CH$_2$ stretching mode is predominantly aligned in the plane of the molecule (38,39). The consistent orientation of the symmetric CH$_2$ mode in the cholesterol molecule complies with the strong polarization dependence observed. The polarization dependence of the 2945 cm^{-1} mode is orthogonal to the polarization dependence of the symmetric CH$_2$ stretch, indicating that polarizability direction of this mode is orthogonal to the symmetric CH$_2$ mode. Despite the spectral changes due to the orientation of the cholesterol crystals, the Raman spectral markers occur at fixed frequencies, thus enabling a confident detection of randomly oriented ChCs in atherosclerotic plaques with hyperspectral SRS microscopy.

In addition to their strong SRS signal, ChC can also be visualized based on its nonvanishing second-order nonlinearity with SHG microscopy (Figs. 2, 3, and 6). Whereas SRS detects ChC based on the C-H vibrational contrast, the SHG signal from ChC arises from the noncentrosymmetry of the chiral cholesterol molecules in the crystal lattice, giving rise to a finite second-order susceptibility (40). Accordingly, the SHG signal can be used to assess the crystallinity of condensed ChC structures in the aorta. Our studies confirm the SHG-activity of crystallized cholesterol. Additionally, the SHG signal from these crystals was found to be polarization-sensitive, further corroborating the ordered crystalline structure of the materials identified as ChC (Fig. 3). We found that other ordered structures in the plaque, including needles of cholesteryl esters, also produced nonvanishing SHG signals. Similarly, protein crystals and ordered structural proteins such as fibrous collagen exhibit significant SHG signals, as shown in numerous studies (29,40–42). Therefore, although SHG imaging provides useful information about the crystallinity of the structures found in atherosclerotic lesions, this modality alone is insufficient to exclusively identify ChC. The use of hyperspectral coherent Raman microscopy proved essential for the reliable detection of ChC.

Most of the crystallized structures shown in this study were located near the ascending and aortic arch regions of the ApoE-deficient mouse aorta, consistent with previous findings (11,19,20). The length of these crystals ranges from 4 μm for a single needle up to 50 μm for an agglomeration of plates. Among these crystals, we identified different classes of cholesterol, including cholesterol monohydrate, cholesteryl oleate, and cholesteryl linoleate—known as key lipids in atherogenesis (43,44). The structures identified as ChC, as expected, exhibit strong SHG activity. In contrast, structures with amorphous morphologies and spectral signatures other than ChC, did not exhibit a strong SHG signal or polarization dependence. Structures with the latter properties can be ruled out as being ChC. For example, the amorphous circular structure adjacent to the plate in

Fig. 5, exhibits cholesterol spectral signatures but virtually no SHG activity; we attribute these structures to liquid, noncrystalline, cholesterol. Given the fast imaging speed and compatibility of SHG with the coherent Raman platform, SHG stands out as a suitable NLO partner for SRS to discriminate crystalline structures such as ChC from amorphous components in the plaque, obviating additional morphological assessment that can be subjective at times. The fast imaging speed of SHG is also useful for sample browsing of large tissue area and can help guide the microscopist to locate the presence of crystallized materials and collagen in the lesion. Subsequently, hyperspectral SRS can be utilized to study the specific composition of the crystallized materials.

Combined SRS and SHG imaging enables a clear separation between lipophilic compounds and other tissue materials. For instance, collagen is ubiquitous in aortic tissue and produces strong signals in both the SRS and SHG channels (29,41), but can be accurately discriminated from lipid-type structures. Additionally, micrometer needle-shaped structures with spectra characteristic of structural protein was found in the aorta as well (28). Interestingly, these protein-needles also exhibit a strong SHG signal and polarization dependence (data not shown), which can be attributed to highly condensed structural proteins or protein crystals (40). Further study is required to determine the origin and role of these protein needles in the plaque.

Out of the three types of ChC observed in this study, cholesterol monohydrate crystals comprise the majority of ChC in the aorta. Moreover, all the plate-shaped crystals are composed of cholesterol monohydrate, whereas the composition of the needle-shaped crystals varies, in agreement with several in vitro studies (45–47). The prevalence of cholesterol monohydrate crystals is also consistent with previous observations in atherosclerotic lesions and other pathologies such as lithogenic bile (46,48). In this regard, several studies have suggested the contribution of cholesterol-rich erythrocyte membrane to the accumulation of free-cholesterol and subsequent crystallization in the plaque (7,49). Solomonov et al. (50) have shown the importance of sterol-water interface in ChC formation within cell membranes, supporting the hypothesis of cholesterol monohydrate crystallization within the erythrocyte membrane. A recent study by Rajamäki et al. (10) has shown that macrophages, which ingest ChC, are also capable of storing the partially digested ChC monohydrates as cholesteryl-esters. Such occurrence may be responsible for the crystallization of cholesteryl-esters and may potentially explain the lower abundance of cholesteryl-ester crystals in this study. A more comprehensive investigation, involving a time-series characterization of ChC in mice in different diet regimes, is required to further our understanding of the origin and role of various ChC materials in atherosclerosis. The precise identification and quantification of ChC with NLO techniques may prove indispensable for such investigations.

CONCLUSION

Previous studies have inferred the presence of ChC in tissue based on its solidlike morphology. To better understand the physiochemical origin of ChC, its specific role in plaque vulnerability and potential use as a biomarker for atheroprogression, a chemically selective tool that can probe ChC within its native cellular milieu is a prerequisite. In this study, we utilized two NLO imaging modalities, SHG and hyperspectral SRS microscopy, to interrogate the composition of solidlike structures in aortas of diseased mice. We found that despite the polarization dependence of the ChC Raman spectrum, the distinct spectral signatures permit a reliable identification of cholesterol monohydrate crystals. Moreover, the spectral analysis enabled by hyperspectral SRS imaging allows discrimination of cholesterol monohydrate crystals from other condensed structures in the tissue, including condensed cholesteryl esters. In addition, we observed SHG activity from plate- and needle-shaped solids within intact plaques, corroborating the crystallinity of the ChC structures. However, the nonvanishing SHG-activity of other structures in the tissue indicates that SHG microscopy alone is insufficient for identifying ChC materials in atherosclerotic plaques, underlining the merits of a combined hyperspectral SRS and SHG approach.

REFERENCES

1. Badimon, J. J., B. Ibanez, and G. Cimmino. 2009. Genesis and dynamics of atherosclerotic lesions: implications for early detection. *Cerebrovasc. Dis.* 27 (*Suppl 1*):38–47.

2. Lloyd-Jones, D., R. J. Adams, …, J. Wylie-Rosett, WRITING GROUP MEMBERS, American Heart Association Statistics Committee and Stroke Statistics Subcommittee. 2010. Heart disease and stroke statistics—2010 update: a report from the American Heart Association. *Circulation.* 121:e46–e215.

3. Thim, T. 2010. Pathology of Vulnerability Caused by High-Risk (Vulnerable) Arteries and Plaques. Springer Science, New York.

4. Guyton, J. R., and K. F. Klemp. 1994. Development of the atherosclerotic core region. Chemical and ultrastructural analysis of microdissected atherosclerotic lesions from human aorta. *Arterioscler. Thromb.* 14:1305–1314.

5. Chen, Z., M. Ichetovkin, …, E. Hailman. 2010. Cholesterol in human atherosclerotic plaque is a marker for underlying disease state and plaque vulnerability. *Lipids Health Dis.* 9:61–68.

6. Virmani, R., F. D. Kolodgie, …, S. M. Schwartz. 2000. Lessons from sudden coronary death: a comprehensive morphological classification scheme for atherosclerotic lesions. *Arterioscler. Thromb. Vasc. Biol.* 20:1262–1275.

7. Abela, G. S. 2010. Cholesterol crystals piercing the arterial plaque and intima trigger local and systemic inflammation. *J. Clin. Lipidol.* 4:156–164.

8. Abela, G. S., K. Aziz, …, J. Dejong. 2009. Effect of cholesterol crystals on plaques and intima in arteries of patients with acute coronary and cerebrovascular syndromes. *Am. J. Cardiol.* 103:959–968.

9. Abela, G. S. 2010. Role of cholesterol crystals in myocardial infarction and stroke. *Clin. Lipidol.* 5:57–69.

10. Rajamäki, K., J. Lappalainen, …, K. K. Eklund. 2010. Cholesterol crystals activate the NLRP3 inflammasome in human macrophages: a novel link between cholesterol metabolism and inflammation. *PLoS ONE.* 5:e11765.

11. Duewell, P., H. Kono, …, E. Latz. 2010. NLRP3 inflammasomes are required for atherogenesis and activated by cholesterol crystals. *Nature.* 464:1357–1361.

12. Patel, R., A. Janoudi, …, G. S. Abela. 2011. Plaque rupture and thrombosis are reduced by lowering cholesterol levels and crystallization with ezetimibe and are correlated with fluorodeoxyglucose positron emission tomography. *Arterioscler. Thromb. Vasc. Biol.* 31:2007–2014.

13. Badimon, L., R. F. Storey, and G. Vilahur. 2011. Update on lipids, inflammation and atherothrombosis. *Thromb. Haemost.* 105 (*Suppl 1*): S34–S42.

14. Shah, P. K., E. Falk, …, V. Fuster. 1995. Human monocyte-derived macrophages induce collagen breakdown in fibrous caps of atherosclerotic plaques. Potential role of matrix-degrading metalloproteinases and implications for plaque rupture. *Circulation.* 92:1565–1569.

15. Liu, L., J. A. Gardecki, …, G. J. Tearney. 2011. Imaging the subcellular structure of human coronary atherosclerosis using micro-optical coherence tomography. *Nat. Med.* 17:1010–1014.

16. Elle, I. C., L. C. Olsen, …, N. J. Faergeman. 2010. Something worth dyeing for: molecular tools for the dissection of lipid metabolism in *Caenorhabditis elegans. FEBS Lett.* 584:2183–2193.

17. Yue, S. H., M. N. Slipchenko, and J. X. Cheng. 2011. Multimodal nonlinear optical microscopy. *Laser Photonics Rev.* 5:496–512.

18. Min, W., C. W. Freudiger, …, X. S. Xie. 2011. Coherent nonlinear optical imaging: beyond fluorescence microscopy. *Annu. Rev. Phys. Chem.* 62:507–530.

19. Kim, S. H., E. S. Lee, …, D. W. Moon. 2010. Multiplex coherent anti-Stokes Raman spectroscopy images intact atheromatous lesions and concomitantly identifies distinct chemical profiles of atherosclerotic lipids. *Circ. Res.* 106:1332–1341.

20. Lim, R. S., J. L. Suhalim, …, B. J. Tromberg. 2011. Identification of cholesterol crystals in plaques of atherosclerotic mice using hyperspectral CARS imaging. *J. Lipid Res.* 52:2177–2186.

21. Freudiger, C. W., W. Min, …, X. S. Xie. 2008. Label-free biomedical imaging with high sensitivity by stimulated Raman scattering microscopy. *Science.* 322:1857–1861.

22. Brustlein, S., P. Ferrand, …, H. Rigneault. 2011. Optical parametric oscillator-based light source for coherent Raman scattering microscopy: practical overview. *J. Biomed. Opt.* 16:021106.

23. Bégin, S., B. Burgoyne, …, D. Côté. 2011. Coherent anti-Stokes Raman scattering hyperspectral tissue imaging with a wavelength-swept system. *Biomed. Opt. Express.* 2:1296–1306.

24. Lin, C. Y., J. L. Suhalim, …, E. O. Potma. 2011. Picosecond spectral coherent anti-Stokes Raman scattering imaging with principal component analysis of meibomian glands. *J. Biomed. Opt.* 16:021104.

25. Ringnér, M. 2008. What is principal component analysis? *Nat. Biotechnol.* 26:303–304.

26. Miljković, M., T. Chernenko, …, M. Diem. 2010. Label-free imaging of human cells: algorithms for image reconstruction of Raman hyperspectral datasets. *Analyst (Lond.).* 135:2002–2013.

27. Pliss, A., A. N. Kuzmin, …, P. N. Prasad. 2010. Nonlinear optical imaging and Raman microspectrometry of the cell nucleus throughout the cell cycle. *Biophys. J.* 99:3483–3491.

28. Koljenović, S., T. C. Bakker Schut, …, G. J. Puppels. 2005. Tissue characterization using high wave number Raman spectroscopy. *J. Biomed. Opt.* 10:031116.

29. Lim, R. S., A. Kratzer, …, B. J. Tromberg. 2010. Multimodal CARS microscopy determination of the impact of diet on macrophage infiltration and lipid accumulation on plaque formation in ApoE-deficient mice. *J. Lipid Res.* 51:1729–1737.

30. Potma, E. O., J. X. Cheng, and X. S. Xie. 2011. Coherent Raman imaging techniques and biomedical applications. *J. Biomed. Opt.* 16:021101.

31. Benalcazar, W. A., and S. A. Boppart. 2011. Nonlinear interferometric vibrational imaging for fast label-free visualization of molecular domains in skin. *Anal. Bioanal. Chem.* 400:2817–2825.

32. Chowdary, P. D., W. A. Benalcazar, …, M. Gruebele. 2010. High speed nonlinear interferometric vibrational analysis of lipids by spectral decomposition. *Anal. Chem.* 82:3812–3818.

33. Vartiainen, E. M., H. A. Rinia, …, M. Bonn. 2006. Direct extraction of Raman line-shapes from congested CARS spectra. *Opt. Express.* 14:3622–3630.

34. Liu, Y., Y. J. Lee, and M. T. Cicerone. 2009. Broadband CARS spectral phase retrieval using a time-domain Kramers-Kronig transform. *Opt. Lett.* 34:1363–1365.

35. Faiman, R. 1977. Raman spectroscopic studies of different forms of cholesterol and its derivatives in the crystalline state. *Chem. Phys. Lipids.* 18:84–104.

36. Bresson, S., D. Bormann, and B. Khelifa. 1998. Raman studies of the C-H stretching modes in various cholesteryl alkanoates. *Vib. Spectrosc.* 16:163–171.

37. Tantipolphan, R., T. Rades, …, N. J. Medlicott. 2006. Analysis of lecithin-cholesterol mixtures using Raman spectroscopy. *J. Pharm. Biomed. Anal.* 41:476–484.

38. JMOL: an open-source Java viewer for chemical structures in 3D. Accessed 8 December 2011. <http://www.jmol.org/>.

39. The Free Chemical Database. Royal Society of Chemistry. Accessed 8 December 2011. <http://www.chemspider.com/5775>.

40. Wampler, R. D., D. J. Kissick, …, G. J. Simpson. 2008. Selective detection of protein crystals by second harmonic microscopy. *J. Am. Chem. Soc.* 130:14076–14077.

41. Wang, H. W., I. M. Langohr, …, J. X. Cheng. 2009. Imaging and quantitative analysis of atherosclerotic lesions by CARS-based multimodal nonlinear optical microscopy. *Arterioscler. Thromb. Vasc. Biol.* 29:1342–1348.

42. Campagnola, P. J., A. C. Millard, …, W. A. Mohler. 2002. Three-dimensional high-resolution second-harmonic generation imaging of endogenous structural proteins in biological tissues. *Biophys. J.* 82:493–508.

43. Degirolamo, C., G. S. Shelness, and L. L. Rudel. 2009. LDL cholesteryl oleate as a predictor for atherosclerosis: evidence from human and animal studies on dietary fat. *J. Lipid Res.* 50 (*Suppl*):S434–S439.

44. Leitinger, N. 2003. Cholesteryl ester oxidation products in atherosclerosis. *Mol. Aspects Med.* 24:239–250.

45. Uskoković, V. 2008. Insights into morphological nature of precipitation of cholesterol. *Steroids.* 73:356–369.

46. Konikoff, F. M., A. Kaplun, and T. Gilat. 1999. Imaging and monitoring cholesterol crystallization in bile. *Scanning Microsc.* 13: 381–393.

47. Chung, D. S., G. B. Benedek, …, J. M. Donovan. 1993. Elastic free energy of anisotropic helical ribbons as metastable intermediates in the crystallization of cholesterol. *Proc. Natl. Acad. Sci. USA.* 90:11341–11345.

48. Bogren, H., and K. Larsson. 1963. An x-ray-diffraction study of crystalline cholesterol in some pathological deposits in man. *Biochim. Biophys. Acta.* 75:65–69.

49. Kolodgie, F. D., A. P. Burke, …, R. Virmani. 2007. Free cholesterol in atherosclerotic plaques: where does it come from? *Curr. Opin. Lipidol.* 18:500–507.

50. Solomonov, I., M. J. Weygand, …, L. Leiserowitz. 2005. Trapping crystal nucleation of cholesterol monohydrate: relevance to pathological crystallization. *Biophys. J.* 88:1809–1817.